

Air-cooled LiBr–water absorption chillers for solar air conditioning in extremely hot weathers

D.S. Kim ^{a,*}, C.A. Infante Ferreira ^b

^a Aresnal research, Sustainable Energy Systems, Giefinggasse 2, 1210 Vienna, Austria

^b Delft University of Technology, Engineering Thermodynamics, Leeghwaterstraat 44, 2628 CA Delft, The Netherlands

ARTICLE INFO

Article history:

Received 21 September 2007

Received in revised form 14 July 2008

Accepted 16 December 2008

Available online 25 January 2009

Keywords:

Solar cooling

Absorption

Half-effect cycle

LiBr

Crystallization

Air-cooled chiller

ABSTRACT

A low temperature-driven absorption cycle is theoretically investigated for the development of an air-cooled LiBr–water absorption chiller to be combined with low-cost flat solar collectors for solar air conditioning in hot and dry regions. The cycle works with dilute LiBr–water solutions so that risk of LiBr crystallization is less than for commercially available water-cooled LiBr–water absorption chillers even in extremely hot ambient conditions. Two-phase heat exchangers in the system were modelled taking account of the heat and mass transfer resistances in falling film flows by applying the film theory in thermal and concentration boundary layers. Both directly and indirectly air-cooled chillers were modelled by properly combining component models and boundary conditions in a matrix system and solved with an algebraic equation solver. Simulation results predict that the chillers would deliver chilled water around 7.0 °C with a COP of 0.37 from 90 °C hot water under 35 °C ambient condition. At 50 °C ambient temperature, the chillers retained about 36% of their cooling power at 35 °C ambient. Compared with the directly air-cooled chiller, the indirectly air-cooled chiller presented a cooling power performance reduction of about 30%.

© 2008 Elsevier Ltd. All rights reserved.

1. Introduction

As energy price as well as environmental awareness among the public grows fast, various technologies that utilize renewable or sustainable energy sources are receiving great interest. In refrigeration sector, thermally driven cooling is currently a popular subject, which includes various closed or open sorption cooling technologies working on low-temperature heat sources.

Among other heat sources, sun is probably the oldest and most popular source of the heat for sorption cooling technologies. A sorption cooling machine, as is expected for a thermal system in general, tends to perform better with a higher heat source temperature [1,2]. However, in spite of the technological development in the mean time, the cost of a high-temperature solar collector system is still too high for a high-temperature (-efficiency) solar cooling system (e.g. [3]) to be generally accepted.

Currently most solar cooling systems are based on water-cooled single-effect absorption chillers followed by adsorption chillers and liquid or solid desiccant machines, whose driving temperatures are in the vicinity of 90 °C [2,4]. Since the cost of a solar collector system, which is normally the largest in the total budget, is proportional to its working temperature, low temperature-driven

sorption machines [5–9] might have a chance to further cut down the initial investment cost of a water-cooled system.

Regarding cost reduction, the same would hold for an air-cooled solar cooling system. However, since the driving temperature of an air-cooled sorption machine is very likely to be beyond 100 °C, reduced driving temperature would benefit especially an air-cooled system by negating pressurization of water or circulation of a non-volatile heat transfer medium in a solar system as well as allowing increased solar collector efficiency. In the past, a few low temperature-driven air-cooled absorption cycles were investigated in this respect [10–12].

Kim and Machielsen [10] carried out simulations of various absorption cycles under solar cooling conditions and concluded that a half-effect LiBr–water cycle would be most promising for air-cooled solar absorption air conditioning in terms of initial solar collector cost, which was attributable to the excellent thermodynamic properties of the working fluids and the low driving temperature requirement of the half-effect absorption cycle.

Izquierdo et al. [11,12] investigated a double-stage LiBr–water absorption cycle for air-cooled solar air conditioning and drew a similar conclusion. They focused on the risk of local LiBr crystallization in the cycle under air-cooled conditions and concluded that crystallization would occur if the lowest absorption temperature is increased beyond 50 °C. This temperature limit is, however, practically the same as the operating limit of conventional (single- or double-effect) air-cooled LiBr–water machines [13–15], which is

* Corresponding author. Tel.: +43 50 550 6668; fax: +43 50 550 6613.

E-mail address: Dong-Seon.Kim@arsenal.ac.at (D.S. Kim).

Nomenclature

A	area, m ²	Δ_T	thermal boundary layer thickness at the interface, m
a	constant in Eq. (16)	Δ_x	concentration boundary layer thickness at the interface, m
C_p	heat capacity, kJ kg ⁻¹ K ⁻¹	δ	film thickness, m
c_{1-3}	constants in Eqs. (14) and (15)	μ	dynamic viscosity, Pa s
D	mass diffusivity, m ² s ⁻¹	ρ	density, kg m ⁻³
h	specific enthalpy, kJ kg ⁻¹	Φ_h	correction factor for interface heat transfer (Ackermann factor) in Eq. (9)
h^{fg}	latent heat, kJ kg ⁻¹	ϕ_h	dimensionless thermal mass flux, $\phi_h \equiv \dot{n}^i C_p / \alpha^i = 1 / St_h$
k	thermal conductivity, kW m ⁻¹ K ⁻¹	Φ_m	correction factor for mass transfer as defined in Eq. (7)
L	absorber length, m	ϕ_m	dimensionless mass flux, $\phi_m \equiv \dot{n}^i / (\rho \beta) = 1 / St_m$
Le	Lewis number, $(k / \rho C_p) / D$		
\dot{m}	mass flow rate, kg s ⁻¹	Superscripts	
n	exponent of Lewis number in Eq. (11)	b	bulk solution
\dot{n}	mass flux, kg m ⁻² s ⁻¹	i	vapour–liquid interface
p	pressure, kPa	w	wall
\dot{Q}	heat flow rate, kW	l	liquid
\dot{q}	heat flux, kW m ⁻²	s	saturated or equilibrium
Re_f	film Reynolds number, $4\Gamma / \mu$	v	vapour
St_h	Stanton number for interface heat transfer, $\alpha^i / \dot{n}^i C_p$	$*$	dew point
St_m	Stanton number for mass transfer, $\rho \beta / \dot{n}^i$	Subscripts	
T	temperature of solution and vapour, K	o	reference condition
t	temperature of cooling water, K	h	heat transfer
U	average overall heat transfer coefficient, kW m ⁻² K ⁻¹	j	grid index
x	mass fraction of absorbent in solution	m	mass transfer
y	distance perpendicular to flow direction, m	s	solution
z	distance in flow direction, m	sub	subcooling
		v	vapour
Greek symbols		w	water
α	average heat transfer coefficient, kW m ⁻² K ⁻¹		
β	average mass transfer coefficient, m s ⁻¹		
Γ	flow rate per unit perimeter, kg/ms		
ΔA	heat transfer area in a control volume, m ²		
Δh	heat of absorption ($\Delta h = a h^{fg}$), kJ kg ⁻¹		
ΔT	temperature difference, K		

considered too low for a reasonably sized air-cooled absorber to perform effectively in hot weathers. Considering that a practical machine should be designed to operate far away from this limit to avoid accidental crystallization, it is questionable if an air-cooled LiBr–water chiller based on such a cycle would perform well in a hot climate.

It is noted that Arivazhagan et al. [7] suggested using an organic working pair (R134a–DMAC) for the same absorption cycle as mentioned by Izquierdo et al. [11,12] to reduce the driving temperature of solar refrigeration systems. The authors claimed that an average increase of 33% in COP was feasible with the proposed working pair in comparison with that of ammonia–water. A comparison with the working pair LiBr–water is unfortunately not given. The main disadvantages of this organic working pair are the need of rectification and the flammability and toxicity of the absorbent.

In this study, it will be shown that a particular type of half-effect air-cooled LiBr–water absorption chiller could work effectively in an extremely hot climate with little risk of crystallization. In comparison with high-temperature air-cooled absorption chillers [16,17], the chiller described in the present study is regarded advantageous for the development of a low-cost air-cooled solar cooling system by allowing cheaper flat solar collectors to be used.

2. Heat-coupled half-effect parallel-flow LiBr–water absorption chiller

The absorption refrigeration cycle considered in this study is described in the following.

Fig. 1 shows block and p–T–x diagrams of the cycle. The numerical indices in the process description refer to the points in Fig. 1a.

As shown in Fig. 1b, the cycle has three system pressures, namely high pressure p_H , mid-pressure p_M and low-pressure p_L . At each pressure level, there is a pair of components, i.e. a generator and a condenser at p_H , MPE (Mid-Pressure Evaporator) and MPA (Mid-Pressure Absorber) at p_M and LPE (Low-Pressure Evaporator) and LPA (Low-Pressure Absorber) at p_L .

From the outlet of a solution tank (point 14 in Fig. 1a), a solution pump delivers refrigerant-rich solution to the generator via HT-SHX (High-Temperature Solution Heat eXchanger, 14 → 16). In the generator, the rich solution is boiled (16 → 24) by the heating medium (35 → 36) from solar collectors and the resulting steam is supplied to the condenser (25).

The liquefied refrigerant from the condenser (3) goes through Ref-Hex (3 → 4) to a refrigerant tank (4 → 8) and is split into two streams with one part supplied to LPE (7) and the other to MPE (6), where the refrigerant is evaporated to be absorbed in LPA (19 → 18) and MPA (22 → 21), respectively. Only the evaporation in LPE (7 → 1) delivers cooling effect. MPE (6 → 2) is in direct thermal contact with LPA (19 → 18) to remove the absorption heat. Ref-Hex reduces flash evaporation by cooling down the refrigerant (3 → 4) from the condenser with the cold solution (18 → 5) from LPA.

On the other hand, hot and refrigerant-poor solution at the outlet of generator (24) is split into two streams after HT-SHX (24 → 23) with one part supplied to MPA (22) and the other to LPA (19) via LT-SHX (Low-Temperature Solution Heat eXchanger, 23 → 19). The poor solution absorbs vapour while being cooled

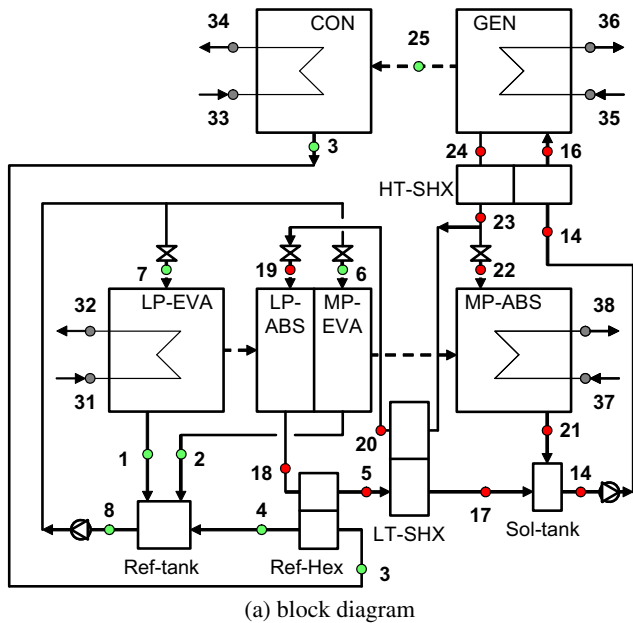


Fig. 1. Heat-coupled parallel-flow cycle.

by the coolant flow in MPA (37 → 38) and the evaporating refrigerant flow in MPE (6 → 2), respectively.

The rich solution after LPA (18) goes through Ref-Hex (18 → 5) and then LT-SHX (5 → 17) to the solution tank to join the other rich solution stream from MPA (21).

As already mentioned, MPE (6 → 2) is in direct thermal contact, i.e. 'heat-coupled', with LPA (19 → 18) to reject the absorption heat at a much lower temperature than that of ambient so that the maximum temperature in the generator (24) can be significantly lower than in a conventional cycle.

This cycle has been named as 'heat-couple parallel-flow' to differentiate it from other similar cycles such as in Fig. 2.

First of all, if the poor solution after the generator is supplied to MPA and then to LPA in series, the cycle would look like Fig. 2a and be called 'serial-flow'. In spite of this difference, the COP and the maximum generator temperature would be roughly the same.

Fig. 2b is the cycle considered in Izquierdo et al. [11,12]. Actually, it is a combination of two single-effect cycles where the absorber of one cycle (MP-ABS in Fig. 2b) is 'mass-coupled' with the generator of the other (MP-GEN) in terms of vapour flow between them. This cycle is similar to the cycles in Figs. 1 and 2a in terms of COP and the maximum generator temperature. However, heat rejection temperature of the low-pressure absorber (LP-ABS) in Fig. 2b is much higher than that of Fig. 2a (i.e. absorbent concentra-

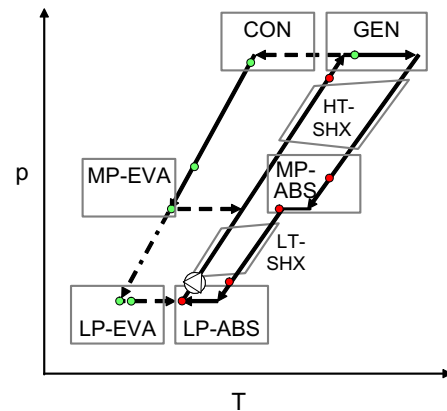


Fig. 2. Other half-effect cycles.

tion is high) and thus it is exposed to a higher risk of crystallization when LiBr–water solution is used as a working fluid under air-cooled conditions.

COPs of the LiBr–water half-effect cycles range between 0.3 and 0.4. Driving temperature is typically in the range of 60–70 °C in water-cooled conditions and it is 20–30° higher in air-cooled conditions.

Fig. 3 shows schematic diagrams of the heat exchangers used in an indirectly air-cooled half-effect parallel-flow LiBr–water absorption chiller [18].

In Fig. 3a, the generator–condenser unit consists of a shell-and-tube type generator and a shell-and-coil type condenser. The absorber–evaporator unit in Fig. 3b includes two pairs of absorber and evaporator in a single pressure vessel. First of all, the vessel is divided into two compartments, i.e. low- and mid-pressure, by

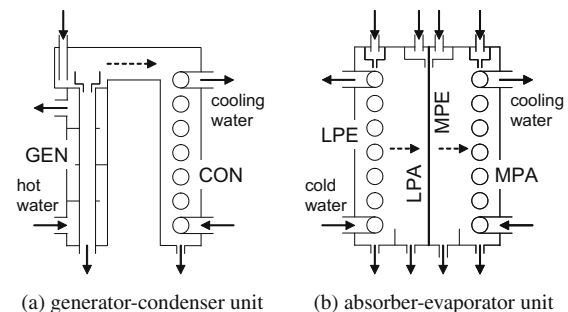


Fig. 3. Indirect air-cooled design (—: liquid, --: vapour).

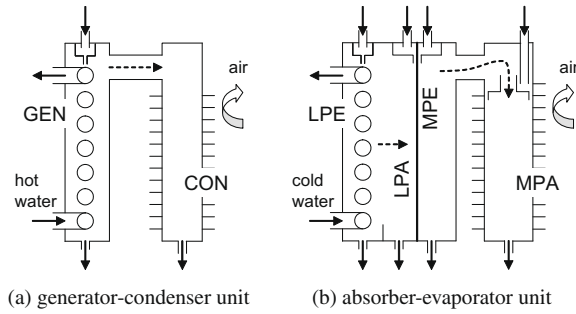


Fig. 4. Direct air-cooled designs (—: liquid, ---: vapour).

a thin vertical wall (denoted by 'LPA/MPE unit' from here on), on one side of which flows poor solution (LPA) and on the other flows water (MPE). The spiral tube falling film heat exchangers in low- and mid-pressure compartment are LPE and MPA, respectively.

Advantage of the indirect air-cooled design in Fig. 3 is that a chiller can be easily built with normal shell-and-tube or coil heat exchangers. Disadvantage is that since the condenser and MPA cannot be directly cooled with air, a dry cooler is required for cooling down a secondary heat transfer medium.

For a direct air-cooled design, fin-and-tube heat exchangers [13,14] may be used for condenser and MPA as shown in Fig. 4.

An indirect air-cooled chiller will require more electric power and a higher driving temperature than a direct one. Nevertheless both designs will be considered in the further discussion.

In the following, all falling film heat exchangers are assumed counter-current except for the LPA/MPE unit. The modelling method is explained in the next section taking the absorber as example.

3. Modelling of falling film heat exchangers

Fig. 5 shows a schematic diagram of an absorber, which is divided into n elements in the direction of solution flow. Governing equations are derived and simplified as follows. Models of the other falling film heat exchangers are similar and their details can be found in [18].

Conservation laws applied to the j th control volume element in Fig. 5 give the following governing equations.

Total mass balance:

$$\sum \dot{m} = \dot{m}_j + \dot{n}^i \Delta A_j - \dot{m}_{j+1} = 0 \quad (1)$$

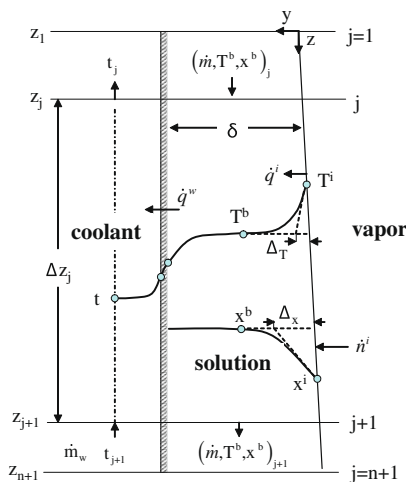


Fig. 5. Control volume element in a falling film absorber.

Absorbent mass balance:

$$\sum \dot{m} x = \dot{m}_j x_j^b - \dot{m}_{j+1} x_{j+1}^b = 0 \quad (2)$$

Energy balance on film side:

$$\sum \dot{Q} = \dot{m}_j h_j^l + \dot{n}^i \Delta A_j h^v - \dot{m}_{j+1} h_{j+1}^l - \dot{Q}_j = 0 \quad (3)$$

Energy balance on coolant side:

$$\sum \dot{Q} = \dot{Q}_j - \dot{m}_w c_{p_w} (t_j - t_{j+1}) = 0 \quad (4)$$

where \dot{Q}_j , the heat transfer rate from the bulk solution to the coolant is given by

$$\dot{Q}_j = U \Delta A_j (T^b - t_j) \quad (5)$$

Eqs. (1)–(4) are the conservation equations for bulk flows and require boundary conditions at vapour–liquid interface for solution.

Film theory [19,20] postulates that mass is transferred from the interface to the bulk flow through a thin hypothetical stagnant layer. The temperature and concentration profiles in this layer are distorted by the mass convection into the film, which can be substantially different from those of pure diffusion case when mass flux is high.

According to the film theory, the mass flux at the vapour–liquid interface \dot{n}^i is expressed as

$$\dot{n}^i = \Phi_m \rho \beta (x^b - x^i) \quad (6)$$

where mass transfer coefficient β is defined by $\beta \equiv D/\Delta_x$. Φ_m is a correction factor for the unidirectional mass transfer across the boundary layer Δ_x in Fig. 5, which is defined by

$$\Phi_m = \frac{1}{x^i} \left(\frac{\phi_m}{e^{\phi_m} - 1} \right) \quad (7)$$

where $\phi_m \equiv \dot{n}^i / (\rho \beta) = 1/St_m$. In Eq. (7), Φ_m approaches 1.0 when $\phi_m \rightarrow 0$ and $x^i \rightarrow 1$. That is, mode of mass transfer approaches pure diffusion only when mass flux is small and the solution is concentrated.

Similar to Eq. (6), the heat flux \dot{q}^i from the interface to bulk solution is given by

$$\dot{q}^i = \Phi_h \alpha^i (T^i - T^b) \quad (8)$$

where heat transfer coefficient α is defined by $\alpha^i \equiv k/\Delta_T$. Φ_h is the correction factor for the convection across the boundary layer Δ_T in Fig. 5, which is defined by

$$\Phi_h = \frac{\phi_h}{e^{\phi_h} - 1} \quad (9)$$

where $\phi_h \equiv \dot{n}^i c_p / \alpha^i = 1/St_h$.

Energy balance at the interface is given by

$$\dot{q}^i = \dot{n}^i \Delta h \quad (10)$$

and the heat and mass transfer analogy relates the heat and mass transfer coefficients as

$$\alpha^i / \beta = \rho c_p Le^n \quad (11)$$

Noting Eq. (11), inserting Eq. (6) and (8) into Eq. (10) and rearranging gives

$$x^b - x^i = (C_p Le^n / \Delta h) (\Phi_h / \Phi_m) \times (T^i - T^b) \quad (12)$$

which binds bulk and interface conditions so that energy and mass balances are satisfied at the interface.

Note that Eq. (12) is equivalent to the model in [21], which becomes that of [22] when $\Phi_m = \Phi_h = 1$. For the exponent of Lewis number, $n = 0.5$ has been used as given by [22], which is also within $0.5 \leq n \leq 0.6$ given by [21].

Expanding an equilibrium equation of LiBr–water solution in Taylor series and taking only linear terms gives T^i as

$$T^i = \left(\frac{\partial T^s}{\partial x} \right) (x^i - x_o) + \left(\frac{\partial T^s}{\partial T^*} \right) (T^* - T_o^*) + T_o^* \quad (13)$$

where T_o^* is the equilibrium solution temperature defined at x_o and $p(T_o^*)$.

Letting $x_o = x^b$ in Eq. (13) and inserting it into Eq. (12) gives x^i as

$$x^i = x^b - c_1(T^b - T^s) - c_2(T^* - T_o^*) \quad (14)$$

where $T^s = T^s(x^b, p)$, $c_1 = -1/[(\partial T^s/\partial x) + (\Phi_m/\Phi_h)\Delta h/(C_p Le^n)]$ and $c_2 = -c_1(\partial T^s/\partial T^*)$. Replacing T^s with $T^s = (\partial T^s/\partial x)(x^b - x_o) + T_o^*$ in Eq. (14) and inserting it into Eq. (6) gives a function for \dot{m}^i as

$$\dot{m}^i = \Phi_m \rho \beta [c_1 T^b + c_2 T^* + c_3 x^b + c_4] \quad (15)$$

where $c_3 = -c_1(\partial T^s/\partial x)$ and $c_4 = -c_1 T_o^* - c_2 T_o^* - c_3 x_o$.

In this study, the correction factors in Eqs. (7) and (9) were set to unity to simplify the problem consequently assuming pure diffusion in the mass transport process.

Eq. (3) normally requires an iterative technique for solution because solution enthalpy is often given as a complex function of temperature and concentration. It would be convenient if it can be rewritten explicitly in terms of unknowns in a simple form.

Firstly, as shown in [23], the latent heat of solution or heat of absorption Δh can be approximated by

$$\Delta h = a \times h^{fg} \quad (16)$$

where h^{fg} is the latent heat of saturated steam and a is the slope of the $1/T^* - 1/T^s$ curve for a constant concentration, which is expressed as

$$a = \frac{\partial(1/T^*)}{\partial(1/T^s)} \quad (17)$$

Using Eq. (16) Eq. (3) can be rewritten as

$$\dot{m}_j C_{p_s} (T_j^b - T_{j+1}^b) + (\dot{m}_{j+1} - \dot{m}_j) [a h^{fg} + C_{p_s} \Delta T^s - C_{p_v} \Delta T^v] - \dot{Q}_j = \Delta \dot{Q}_j \quad (18)$$

where ΔT^s and ΔT^v are the subcooling of bulk solution and vapour relative to the saturation temperature of the bulk solution defined by $\Delta T^s = [T^s(x^b, p) - T_{j+1}^b]$ and $\Delta T^v = [T^s(x^b, p) - T_{j+1}^v]$, respectively. $\Delta \dot{Q}_j$ on the right-hand side is a residual term for the error of the expression on the left-hand side, which is less than 1% of \dot{Q}_j for the absorption or generation of LiBr–water solutions in the ranges of $0.5 < x^b < 0.7$ and $5^\circ\text{C} < T^* < 50^\circ\text{C}$.

In the four governing equations above, i.e. Eqs. (1), (2), (4), and (18), five unknowns, namely t , T^b , x^b , \dot{m} and T^* , are identified. Since the dew temperature T^* , i.e. the pressure in an absorber is determined in such a way that it should satisfy a mass balance equation between the absorber and a vapour source connected to it (e.g. generator or evaporator), this system can be solved only when either a pressure or absorbed vapour mass is given.

Given a working pressure, an absorber model with n differential elements requires solution of a matrix system formed by $4n$ equations and 4 boundary conditions such as

$$[A][B] = [C] \quad (19)$$

where $[A]$ is a $4(n+1) \times 4(n+1)$ coefficient matrix, $[B]$ is a $4(n+1) \times 1$ column matrix for unknowns and $[C]$ is a $4(n+1) \times 1$ column matrix for residuals and boundary conditions.

Fig. 6 shows an example solution for a water-cooled absorber. Note the rapid changes in the temperature and concentration profiles of solution in the upper part of the absorber ($z/L < 0.1$), where very fine grids were used to follow the trends. On the other hand, the profiles are monotonous downstream, where much coarser

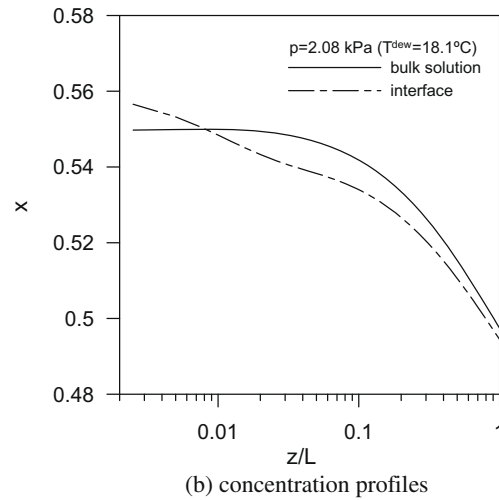
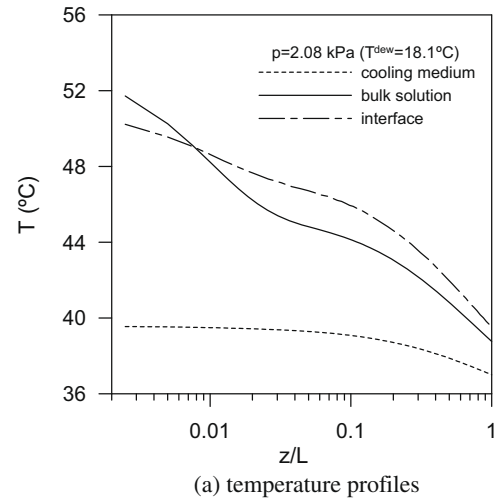


Fig. 6. Temperature and concentration profiles in absorber.

grids were acceptable. For economy of computation, a non-uniform grid system was used. Also note that bulk and interface temperature and concentration profiles cross over at a certain point near inlet ($z/L < 0.007$), which means that vapour is being generated until this point. This is due to the 'supersaturated' state of the solution before the absorber inlet and therefore similar to flash evaporation. A reverse process takes place in a generator supplied with subcooled solution.

For the purpose of validation, the present model was used to simulate the absorber in [24], where absorption test results were reported for the falling film flows inside of a 400 mm-long ϕ 19.05 mm (inside diameter 16.05 mm) copper tube in film Reynolds number range from 50 to 550 using 53 wt% aqueous LiBr solution, and the simulation results were compared with the experimental data. For simulation, the present model requires knowledge of transfer coefficients. The following values have been obtained from Takamatsu et al.'s data [24].

$$\alpha^b = 3.88 \text{Re}_f^{-0.131} \quad (20)$$

$$\beta = 6.26 \times 10^{-4} \text{Re}_f^{-0.143} \quad (21)$$

where α^b is the heat transfer coefficient between tube wall and bulk solution and β is mass transfer coefficient at the vapour–liquid interface. Eqs. (20) and (21) reproduce the heat and mass transfer coefficients of the absorbing film flows in $\text{Re}_f = 130\text{--}560$ in [24]

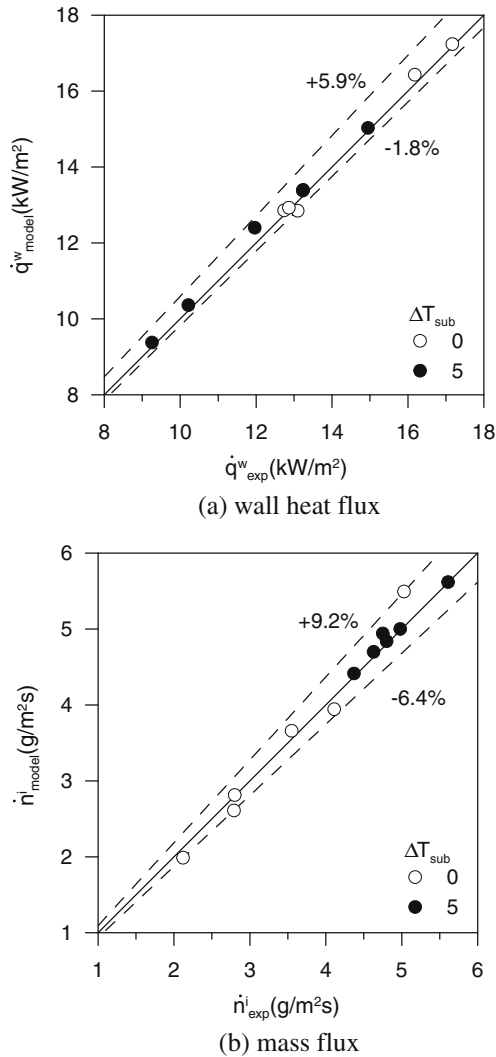


Fig. 7. Comparison with the experimental data from [24].

with a standard deviation of 2.3% and 12.4% (maximum deviation of 4.4% and 19.3%), respectively.

Using Eqs. (20) and (21), the absorber in [24] was simulated for each of the experimental cases with film Reynolds numbers above 100 for two different inlet conditions (0 and 5 K-subcooling) and the results are presented in Fig. 7.

Fig. 7a shows simulated and experimental average heat flux that is transferred through the absorber wall to cooling water. Sim-

ulation results are in excellent agreement with experimental data showing a maximum deviation of only 5.9%. It is notable that heat flux is generally larger with 0 K-subcooling cases.

Fig. 7b shows corresponding mass fluxes at the vapour–liquid interface. Discrepancy is somewhat larger than heat flux cases showing a maximum deviation of 9.2%. This time, mass flux is generally larger with 5 K-subcooling cases.

For the results in Fig. 7, corresponding maximum deviations of the simulation in outlet solution temperature and concentration are 0.45 K and 0.09 LiBwt%, respectively. All in all, Fig. 7 shows an excellent agreement between simulation and experimental data supporting that the present model can simulate an absorber with a high accuracy.

4. System modelling and solution

As shown in Fig. 1, various components are interconnected in the half-effect chiller to transport heat and/or masses between them. Conservation laws should also be satisfied for those interconnected components as well as for a single component. System models were developed by extending a matrix equation such as in Eq. (19) to include all the governing equations of individual component, inter-component conservation equations and boundary conditions. Since the system was non-linear, solution was obtained for N unknowns by solving an $N \times (N + 1)$ augmented matrix using Cholesky's method (see e.g. [25]) renewing the coefficient matrix after each iteration until convergence criteria were met.

Table 1 summarizes some design parameters for an indirect air-cooled system with a cooling power of ca.10 kW (see [18] for examples of the component designs).

All falling film heat exchangers are given specific heat and mass transfer areas and appropriate transfer coefficients, which are expressed in terms of UA and βA values in Table 1. In some components, flow rates of working fluid are variables and cannot be fixed at constant values. All single-phase heat exchangers are modelled as counter-current heat exchangers with constant effectiveness.

In a direct air-cooled system, the UA values of condenser (CON) and mid-pressure absorber (MPA) are assumed to be the same. The same flow rate of air as used in the dry cooler cools down MPA firstly and then CON.

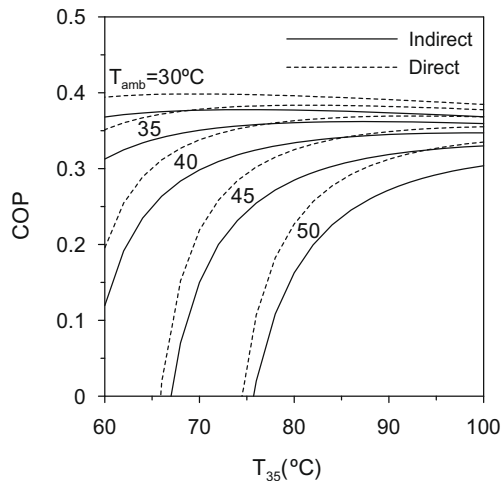
In the following section, some simulation results will be presented for these two systems.

5. Results and discussion

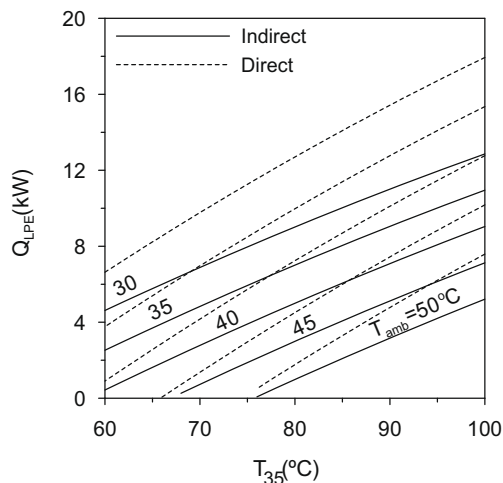
Fig. 8 shows COP and cooling power curves of the direct and indirect air-cooled chillers for different ambient temperature

Table 1
Design parameters for an indirectly air-cooled chiller.

Component	$U \times A$ (kW/K)	$\beta \times A$ (m ³ /s)	Flow rate (kg/s)		Remark
			Hot	Cold	
CON	6.1	–	m_{03}	0.67	1. All flow rates measured at the inlets 2. In a direct air-cooled system, the same CON and MPA are cooled directly with 3.33 kg/s of air 3. m_{03} , m_{24} and m_{18} are variables 4. Effectiveness assumed constant
GEN	6.6	1.9×10^{-3}	1	0.11	
MPA	3.3	1.1×10^{-3}	$0.5 \times m_{24}$	0.67	
LPA	4.0	1.1×10^{-3}	$0.5 \times m_{24}$	0.036	
MPE	–	–	–	–	
LPE	2.9	–	0.42	0.046	
Effectiveness					
HT-SHX	0.8	–	m_{24}	0.11	
LT-SHX	0.8	–	$0.5 \times m_{24}$	m_{18}	
Ref-Hex	0.8	–	m_{18}	m_{03}	
Dry cooler	0.625	–	0.67	3.33	



(a) COP vs. hot water temperature



(b) Cooling power vs. hot water temperature

Fig. 8. Influences of ambient temperature on the performance of air-cooled half-effect LiBr–water absorption chillers ($T_{31} = 13^\circ\text{C}$).

conditions. For the results, the chilled water temperature at LPE inlet (point 31 in Fig. 1a) was set constant at 13°C .

In Fig. 8, first of all, it is clearly shown that both COP and cooling power of the direct air-cooled chiller are significantly larger than those of the indirect air-cooled chiller. This is mainly because heat is rejected from the indirect air-cooled chiller by the cooling water from the dry cooler and therefore heat rejection temperature is inevitably higher than that of the direct air-cooled chiller.

In Fig. 8a, COP increases sharply with increasing hot water temperature near the minimum operating temperature but it slows down afterwards. Cooling power, however, increases almost linearly with increasing hot water temperature in Fig. 8b. For 90°C hot water temperature, COP and cooling power at 35°C ambient temperature are 0.38 and 12.8 kW (chilled water temperature $13 \rightarrow 5.7^\circ\text{C}$) for the direct air-cooled chiller and 0.36 and 9 kW (chilled water temperature $13 \rightarrow 7.8^\circ\text{C}$) for the indirect chiller. Considering a flat plate solar collector producing 90°C hot water at 50% efficiency [4], an overall solar cooling efficiency around 18% would be feasible with these chillers.

It can be seen that for an ambient temperature, there is a minimum operating temperature for a chiller, below which no cooling effect is produced. The minimum operating temperature increases with ambient temperature and for 50°C ambient temperature, it is

approximately 74 and 76°C for the direct and indirect air-cooled chillers, respectively.

It is interesting how effectively these air-cooled chillers operate in high ambient temperature conditions. Fig. 8 shows that even at 50°C ambient temperature, the direct air-cooled chiller can deliver 4.8 kW (37.5% of the cooling power at 35°C ambient) of cooling power with a COP of 0.31 and the indirect chiller can deliver 3.2 kW (35.6% of the cooling power at 35°C ambient) with a COP of 0.27 from 90°C hot water.

Due to the risk of LiBr crystallization, Izquierdo et al. [11,12] suggested that an air-cooled chiller based on their cycle would be limited by 50°C (saturation temperature of 62.3 wt% LiBr–water solution at 0.87 kPa) in its maximum operable ambient temperature. For the chillers considered in this study, however, the operating limit would be much higher because the maximum LiBr concentration inside a chiller varied from 44.5 to 57.4 wt% in Fig. 8.

Although different in system configuration and modelling approach, it may be interesting to compare the present results with those of Izquierdo et al. [11,12]. Fig. 9 shows COP curves of the direct air-cooled chiller in this study and those of [11,12].

In Fig. 9, COP curves from both studies look similar as COP rapidly increases with increasing hot water temperature from a cut-off temperature and slows down to level off. Differences are firstly, the absolute magnitude of maximum COP and secondly, the gradient of a curve in the increasing section. The maximum COPs from [11,12] appear to be 10–20% larger than the present results. Although not clear since it was not specified in [11,12], this is probably due to the differences in system design, mainly in heat exchanger sizes (effectiveness). As regards to the steep gradients of [11,12], a rapidly increasing trend of COP beyond a cut-off temperature is a typical behaviour of an equilibrium model that does not take account of the various heat and mass transfer resistances in a real machine. Note that the curves from [11,12] are based on condenser (dew) temperature and those of this study are on ambient temperature.

The effective operability in extremely hot weather conditions and the reduced risk of crystallization make the chillers considered in this study particularly suitable for air-cooled solar absorption cooling systems in hot and dry regions where a closed system is preferred due to the scarcity of water. Performance of the chillers in Fig. 8 could also be greatly improved if dehumidification load is small so that chilled water temperature can be increased to a higher level [17,26,27].

In all aspects, a direct air-cooled chiller is preferable to an indirect one. However, it would be a big challenge to make a cheap and

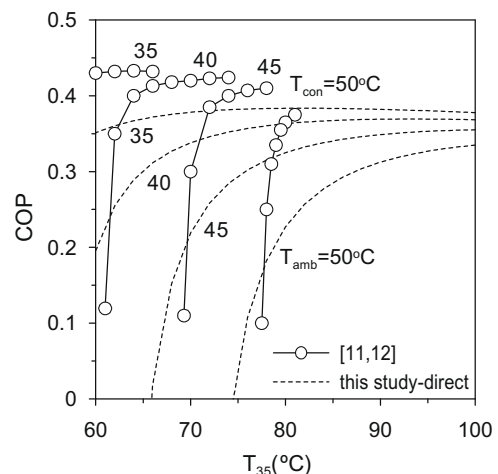


Fig. 9. Comparison with the simulation data from [11,12].

efficient air-cooled absorber. In case of a fin-and-tube type absorber, poor heat and mass transfer of the LiBr–water film inside a tube has been a problem [13,14]. Another critical component is the LPA/MPE unit, which is a vertical wall with falling film flows on both sides in Figs. 3b and 4b. A parametric analysis showed that it is most effective to improve this component for better chiller performance [18].

Regarding manufacturing cost, the heat-coupled parallel-flow cycle in Fig. 1 is also regarded advantageous over the mass-coupled cycle in Fig. 2b. Firstly, the cycle in Fig. 2b requires roughly double the size of an air-cooled absorber of the cycle in Fig. 1 and secondly, it requires one more solution pump. Even compared with a conventional single-effect cycle, the cycle in Fig. 1 requires as extra equipment only the LPA/MPE unit, which is actually a thin vertical heat-conductive wall, and two single-phase heat exchangers as extra.

6. Conclusions

A heat-coupled half-effect parallel-flow absorption cycle has been theoretically investigated for the feasibility of low temperature-driven air-cooled LiBr–water absorption chillers for solar air conditioning in hot weathers. The thermodynamic processes in the cycle and two possible chiller configurations were described. Two-phase heat exchangers in the chillers were modelled taking account of the transfer resistances in simultaneous heat and mass transfer processes by applying the film theory to the boundary layers in falling film flows. System modelling and solution methods were also briefly described. Some simulation results were presented and discussed focusing on the influences of ambient and driving temperatures on the performance of the chillers. From the results, the following conclusions were obtained.

The direct and indirect air-cooled chillers considered in this study are able to deliver chilled water at 5.7 °C and 7.8 °C with a COP of 0.38 and 0.36, respectively, from 90 °C hot water under 35 °C ambient temperature condition.

At 50 °C ambient temperature, COP and cooling power of the direct air-cooled chiller are reduced to 81.6% and 37.5% of those at 35 °C and the reductions are greater for the indirect air-cooled chiller being 75% and 35.6%, respectively.

Risks of LiBr crystallization in the chillers are less than that of a commercial water-cooled machine for hot water temperature up to 100 °C and ambient temperature up to 50 °C when chilled water return temperature is maintained at 13 °C.

Direct air-cooled chiller design is preferable in terms of energy efficiency. It would be, however, challenging to develop cheap and efficient air-cooled condenser and absorber in conventional fin-and-tube heat exchanger designs.

References

- [1] Tozer RM, James RW. Fundamental thermodynamics of ideal absorption cycles. *Int J Refrig* 1997;20:120–35.

- [2] Balaras CA, Grossman G, Henning HM, Infante Ferreira CA, Podesser E, Wang L, et al. Solar air conditioning in Europe – an overview. *Renew Sustain Energy Rev* 2007;11:299–314.
- [3] Lokurlu A, Müller G. Experiences with the worldwide first solar cooling system based on trough collectors combined with double effect absorption chillers. In: *Proceedings of international conference solar air-conditioning*, Bad Staffelstein, Germany; 2005.
- [4] Kim DS, Infante Ferreira CA. Solar refrigeration options – a state-of-the-art review. *Int J Refrig* 2008;31:3–15.
- [5] Saghiruddin MAS. Economic analysis of two stage dual fluid absorption cycle for optimizing generator temperatures. *Energy Convers Manage* 2001;42:407–37.
- [6] Sumathy K, Huang ZC, Li ZF. Solar absorption cooling with low grade heat source – a strategy of development in South China. *Sol Energy* 2002;72:155–65.
- [7] Arivazhagan S, Murugesan SN, Saravanan R, Renganarayanan S. Simulation studies on R134a–DMAC based half effect absorption cold storage systems. *Energy Convers Manage* 2005;46:1703–13.
- [8] Saha BB, Akisawa MA, Kashiwagi T. Solar/waste heat driven two-stage adsorption chiller: the prototype. *Renew Energy* 2001;23:93–101.
- [9] Gommed K, Grossman G. Experimental investigation of a liquid desiccant system for solar cooling and dehumidification. *Sol Energy* 2007;81:131–8.
- [10] Kim DS, Machielsen CHM. Evaluation of air-cooled solar absorption cooling systems. In: *Proceedings of ISHPC, 2002, Shanghai, China*.
- [11] Izquierdo M, Venegas M, Rodríguez P, Lecuona A. Crystallization as a limit to develop solar air-cooled LiBr–H₂O absorption systems using low-grade heat. *Sol Energy Mater Sol Cells* 2004;81:205–16.
- [12] Izquierdo M, Venegas M, García N, Palacios E. Exergetic analysis of a double stage LiBr–H₂O thermal compressor cooled by air/water and driven by low grade heat. *Energy Convers Manage* 2005;46:1029–42.
- [13] Sawada N, Tanaka T, Ikumi Y, Kobayashi T. Study on air-cooled absorption system for light commercial use. In: *Proceedings of absorption heat pump conference, 1991, Tokyo, Japan*.
- [14] Ogawa M, Hoshida T, Oda Y. Study on heat transfer analysis for the vertical condenser/absorber of an air-cooling absorption chiller/heater. In: *Proceedings of absorption heat pump conference, 1991, Tokyo, Japan*.
- [15] Medrano M, Bourouis M, Coronas A. Absorption of water vapor in the falling film of water–lithium bromide inside a vertical tube at air-cooling thermal conditions. *Int J Therm Sci* 2002;41:891–8.
- [16] Velázquez N, Best R. Methodology for the energy analysis of an air cooled GAX absorption heat pump operated by natural gas and solar energy. *Appl Therm Eng* 2002;22:1089–103.
- [17] Zunft S. Solar-driven sorption cooling in arid regions. *Proceedings of EuroSun 2002 ISES conference, 2002, Bologna, Italy*.
- [18] Kim DS. Solar absorption cooling. Dissertation, Delft University of Technology; 2007.
- [19] Bird RB, Stewart WE, Lightfoot EN. *Transport phenomena*. New York: Wiley; 1965.
- [20] Baehr HD, Stephan K. *Wärme- und stoffübertragung*. 3rd ed. Berlin: Springer-Verlag; 1998.
- [21] Yüksel ML, Schlünder EU. Heat and mass transfer in non-isothermal absorption of gases in falling liquid films part I: experimental determination of heat and mass transfer coefficients. *Chem Eng Process* 1987;22:193–202.
- [22] Nakoryakov VE, Grigoreva NI. Calculation of heat and mass transfer in nonisothermal absorption on the initial portion of a downflowing film [translated from]. *Teoreticheskie Osnovy Khimicheskoi Tekhnologii* 1980;14:483–8.
- [23] Haltenburger Jr W. Enthalpy–concentration charts from vapor pressure data. *Ind Eng Chem* 1939;31:783–6.
- [24] Takamatsu H, Yamashiro H, Takata N, Honda H. Vapor absorption by LiBr aqueous solution in vertical smooth tubes. *Int J Refrig* 2003;26:659–66.
- [25] James ML, Smith GM, Wolford JC. *Applied numerical methods for digital computation*. 3rd ed. New York: Harper & Row Publishers; 1985. p. 178–85.
- [26] Safarik M, Richter L, Mockel F, Kretschmar S. Performance data of a small capacity absorption chiller. In: *Proceedings of international conference solar air-conditioning*, Bad Staffelstein, Germany, 2005.
- [27] Storkenmaier F, Harm M, Schweigler C, Ziegler F, Albers J, Kohlenbach P, et al. Small-capacity water/LiBr absorption chiller for solar cooling and waste-heat driven cooling. In: *Proceedings of international congress of refrigeration*, Washington DC, USA, 2003.